J. Fluid Mech. (1998), *vol.* 369, *pp.* 253–272. Printed in the United Kingdom

© 1998 Cambridge University Press

Highly nonlinear standing water waves with small capillary effect

By WILLIAM W. SCHULTZ[1], JEAN-MARC VANDEN-BROECK[2]†, LEI JIANG[1]‡ AND MARC PERLIN[3]

[1]Department of Mechanical Engineering and Applied Mechanics, University of Michigan, Ann Arbor, MI 48109, USA

[2]Department of Mathematics, University of Wisconsin Madison, WI 53706, USA

[3]Department of Naval Architecture and Marine Engineering, University of Michigan, Ann Arbor, MI 48109, USA

(Received 20 March 1997 and in revised form 18 March 1998)

We calculate spatially and temporally periodic standing waves using a spectral boundary integral method combined with Newton iteration. When surface tension is neglected, the non-monotonic behaviour of global wave properties agrees with previous computations by Mercer & Roberts (1992). New accurate results near the limiting form of gravity waves are obtained by using a non-uniform node distribution. It is shown that the crest angle is smaller than 90° at the largest calculated crest curvature. When a small amount of surface tension is included, the crest form is changed significantly. It is necessary to include surface tension to numerically reproduce the steep standing waves in Taylor's (1953) experiments. Faraday-wave experiments in a large-aspect-ratio rectangular container agree with our computations. This is the first time such high-amplitude, periodic waves appear to have been observed in laboratory conditions. Ripple formation and temporal symmetry breaking in the experiments are discussed.

1. Introduction

Finite-amplitude standing waves in two-dimensional potential flow of infinite depth were first considered by Rayleigh (1915). He neglected the effect of surface tension and calculated a solution to third order as a power series in the wave amplitude. A similar expansion was carried to fifth order by Penney & Price (1952). The effects of finite depth (Tadjbakhsh & Keller 1960; Vanden-Broeck & Schwartz 1981) and of surface tension (Concus 1962; Vanden-Broeck 1984) were later included. Schwartz & Whitney (1981) corrected and improved the expansion of Penney & Price to 25th order. They obtained more accurate results for standing waves of relatively large amplitude in the absence of surface tension. The validity of the expansion procedure used by Schwartz & Whitney was proved by Amick & Toland (1987). The substantial literature on nonlinear water waves, including standing waves, is reviewed

† Present address: School of Mathematics, University of East Anglia, Norwich NR4 7TJ, UK.
‡ Present address: Intel Corp. M/S RA1-305, 5200 NE Elam Young Parkway, Hillsboro, OR 97124, USA.

https://doi.org/10.1017/S0022112098001773 Published online by Cambridge University Press

by Schwartz & Fenton (1982). More recent studies on standing water waves include Mercer & Roberts (1992, 1994) and Tsai & Jeng (1994).

We use a time-marching spectral boundary integral method for potential-flow problems to obtain exponential accuracy (Schultz, Huh & Griffin 1994). Both gravity and surface tension are included in the formulation. As in Mercer & Roberts (1992), we calculate standing waves in water of infinite depth using Newton iteration to find appropriate 'initial conditions' for periodicity. More precisely, we determine the wave profile that reproduces itself after one temporal period such that the spatially periodic free-surface elevation and velocity potential are symmetric and antisymmetric, respectively, about the peak of the standing wave. This more restrictive definition eliminates travelling waves and combination standing/travelling waves (Bridges & Dias 1990) that would otherwise satisfy the spatial and temporal periodicity conditions. Furthermore, the nonlinear standing waves analysed here start from rest (as in all previous nonlinear studies, e.g. Schwartz & Whitney 1981) and at no time in the time cycle is the free surface flat. Starting from rest (§ 3.2) excludes the class of standing waves where the kinetic energy is never zero during the cycle. Recent experimental evidence (Jiang *et al.* 1996) suggests that these standing waves exist in a Faraday wave system.

Using prescribed horizontal nodal movement, we obtain sharper-crested gravity standing waves than those previously calculated by Mercer & Roberts (1992). We show that the temporal period is not a monotonic function of the wave amplitude close to its limiting form, in agreement with Mercer & Roberts (1992). A similar result for travelling waves was obtained by Longuet-Higgins (1975), showing that the highest progressive wave is not the fastest.

Penney & Price (1952) suggested that the limiting standing wave is characterized by a sharp crest of 90°. Taylor's (1953) experimental results showed a near-limiting wave with a crest of nearly 90° and a wave profile similar to that predicted by Penney & Price (1952). We shall show that surface tension has to be included to obtain waves as high as those of Taylor (1953) and our computations without surface tension do not support the conjecture of a 90° crest. Note in passing that Hogan (1980), considering the effect of small surface tension on travelling gravity waves, found a reduced maximum height and monotonically increasing wave properties. While we (and Debiane & Kharif 1996) question this result, we show the opposite effect in standing waves, i.e. the limiting wave height is extended and the non-monotonicity is maintained.

We pose the problem in § 2 for standing waves periodic in space and time and present the formulation and technique in § 3 for spectral computation. Numerical results on steep standing waves without surface tension are presented in § 4 with an emphasis on the limiting wave properties. Surprisingly steep waves can be achieved with only weak capillarity as shown in § 5. Experiments presented in § 6 are generated through Faraday-wave resonance in a large-aspect-ratio tank to maintain periodicity and two-dimensionality, and the results confirm the effect of weak capillarity as predicted by our calculations.

2. Problem formulation

We consider time-periodic two-dimensional potential flow of a fluid of infinite depth bounded above by a free surface. As stated in § 1, we assume the motion to be periodic in the horizontal direction. The dimensionless variables are introduced such that the primary wavenumber k, the acceleration due to gravity g, and the fluid density ρ are all equal to one. Therefore the wavelength λ in the calculation is always

https://doi.org/10.1017/S0022112098001773 Published online by Cambridge University Press

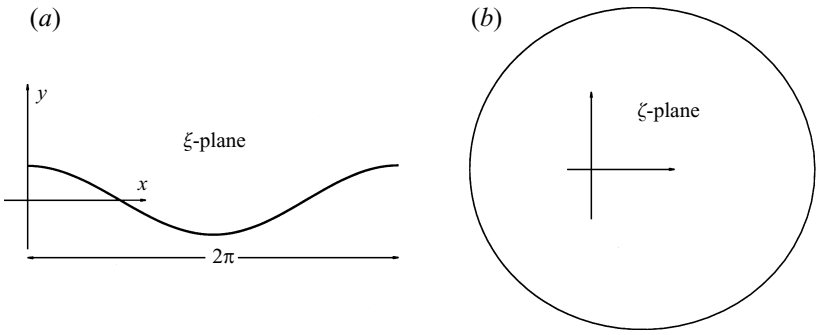


FIGURE 1. (*a*) The physical domain of the problem and (*b*) the mapped computational domain.

2π and the wave height is denoted by H. A Cartesian coordinate system is adopted such that gravity acts in the negative y-direction and the undisturbed surface is $y = 0$ (figure 1*a*).

The fluid motion is described by a complex potential $w(\xi) = \phi + \mathrm{i}\psi$, where ϕ is the velocity potential, ψ is the stream function and $\xi = x + \mathrm{i}y$ represents the two spatial coordinates. At every time step, the unknown boundary values of the velocity potential (half of the values are known from the boundary conditions) are solved using the Cauchy integral formula:

$$\oint_{\partial\Omega} \frac{w(\xi)}{\xi - \zeta_k} \mathrm{d}\xi = \mathrm{i}\alpha w(\zeta_k), \tag{2.1}$$

where α is 0 or 2π if the location of the kernel singularity, ζ_k, is outside or inside the boundary, respectively. If the kernel singularity is on the boundary ($\zeta_k \in \partial\Omega$), α is equal to the included angle, and the integral is treated as principal-valued. For the smooth contour considered here, $\alpha = \pi$.

The kinematic and dynamic boundary conditions on a free surface for an inviscid flow are given as

$$\frac{\mathrm{D}\xi}{\mathrm{D}t} = \frac{\mathrm{d}w^*}{\mathrm{d}\xi} \tag{2.2}$$

and

$$\frac{\mathrm{D}\phi}{\mathrm{D}t} = -y + \frac{1}{2}\left|\frac{\mathrm{d}w^*}{\mathrm{d}\xi}\right|^2 - p. \tag{2.3}$$

Here, * denotes the complex conjugate and $\mathrm{D}/\mathrm{D}t$ is a material derivative. We write the boundary conditions in this form because node locations are often chosen to follow material particles, especially when examining breaking waves (Schultz *et al.* 1994). We often find it desirable to prescribe the horizontal motion of the nodes and hence replace the material derivative above with a derivative $\mathrm{d}/\mathrm{d}t$ that follows a node,

$$\frac{\mathrm{d}}{\mathrm{d}t} = \frac{\mathrm{D}}{\mathrm{D}t} - (\boldsymbol{v} - \boldsymbol{v}_n)\cdot\nabla, \tag{2.4}$$

where $\boldsymbol{v} = \nabla\phi$ is the fluid velocity and $\boldsymbol{v}_n$ is the velocity of the node. These two derivatives are identical when nodes follow material particles. With a prescribed horizontal velocity v_{nx}, the vertical node velocity is calculated by satisfying the kinematic condition (2.2),

$$v_{ny} = v_y + (v_{nx} - v_x)\frac{\partial y}{\partial x}. \tag{2.5}$$

https://doi.org/10.1017/S0022112098001773 Published online by Cambridge University Press

In the case of zero surface tension, we prescribe the horizontal position of the nodes,

$$x_k = \frac{2\pi k}{N} - S \sin\frac{2\pi k}{N} \cos\frac{2\pi t}{T}, \quad k = 1, \cdots, N, \tag{2.6}$$

where S is a 'squeezing factor'. The temporal wave period is denoted by T and the total number of nodes is represented by N. For $S \to 1$, the grid spacing is $\mathcal{O}(1/N^2)$ at the two ends of the domain for $t = 0, T, 2T, \cdots$ and at the middle of the computational domain for $t = \frac{1}{2}T, \frac{3}{2}T, \cdots$. Therefore this nodal distribution $(0 < S < 1)$ provides denser nodes at the crests for gravity-dominated waves with appropriate initial conditions.

The prescribed pressure p in (2.3) is normally zero unless surface tension or wind effects are included. In this study we include surface tension so that

$$p = \frac{1}{Bo} \frac{x'y'' - x''y'}{(x'^2 + y'^2)^{3/2}}, \tag{2.7}$$

where the prime indicates differentiation with respect to a free-surface parameter s. This parameter can be arclength, but as in Baker, Meiron & Orszag (1982), our computations use node number as the parameter. Then, by definition, the parameter is evenly spaced and a Fourier transform is easily applied. The Bond number is given by $Bo = \rho g(k^2\sigma)^{-1}$, where σ is the surface tension coefficient. The inverse Bond number $\kappa = 1/Bo$ is usually very small (for example, $\kappa = 0.0027$ in Taylor's experiments). We show in § 4 and § 5 that this weak capillarity has surprising effects that cannot be neglected at large wave steepness.

We complete the formulation by applying a periodic boundary condition in the horizontal direction, $w(\xi) = w(\xi + 2\pi)$, symmetry conditions at $x = \pi$ for the potential and free surface elevation, the deep water condition $w \to 0$ as $y \to -\infty$, and appropriate initial conditions.

3. Numerical procedure

Based on the kernel desingularization of Roberts (1983), our spectral formulation results in exponentially accurate integration and solutions as shown in Schultz *et al.* (1994). After discretization this leads to a system of nonlinear equations for the unknown initial profile. This system is solved by Newton's method with the Jacobian evaluated numerically by finite differences.

3.1. *Spectral complex-integral method*

The physical domain is mapped to an approximate unit circle (see figure 1*b*) using the conformal transformation:

$$\zeta = \mathrm{e}^{-\mathrm{i}z}. \tag{3.1}$$

This eliminates the periodic boundary conditions and sharp computational corners used by Vinje & Brevig (1981). In the limit of vanishing waves, the mapped domain becomes a unit circle. All derivatives are taken in the spectral space of the conformed representation.

Roberts (1983) used a desingularized kernel in his vortex formulation. Generally, it is difficult to find a suitable desingularized form of a kernel in an integral equation, but in the complex formulation it is relatively simple. The Cauchy integral equation (2.1) can easily be rewritten as

$$\oint \frac{w(s) - w(\zeta_k)}{\xi(s) - \zeta_k} \frac{\mathrm{d}\xi}{\mathrm{d}s} \mathrm{d}s = 0, \tag{3.2}$$

https://doi.org/10.1017/S0022112098001773 Published online by Cambridge University Press

where the principal value integral can be replaced by the closed contour integral since the integrand is no longer singular – when ξ approaches ζ_k, the integrand approaches $\mathrm{d}w/\mathrm{d}s$ at the kth node point. The continuous free-surface parameter s is equal to the node number at each nodal location. The integral equation (3.2) is converted to the following algebraic system:

$$\sum_{j=1}^{N} I_{jk} = 0 \qquad \text{for } k = 1, \ldots, N, \tag{3.3}$$

where N is the number of nodes, and I_{jk} is represented by

$$I_{jk} = \begin{cases} \dfrac{w_j - w_k}{\xi_j - \xi_k} \left(\dfrac{\mathrm{d}\xi}{\mathrm{d}s} \right)_j & \text{if } j \neq k \\ \left(\dfrac{\mathrm{d}w}{\mathrm{d}s} \right)_k & \text{if } j = k. \end{cases} \tag{3.4}$$

The algebraic system (3.4) effectively becomes a differential system because I_{jk} includes the derivative of w. To evaluate these derivatives spectrally, we use a cardinal function representation of w (Boyd 1989):

$$w(s) = \sum_{j=1}^{N} C_j(s) w_j, \tag{3.5}$$

where

$$C_j = \frac{1}{N} \sin \pi(s - s_j) \cot \frac{\pi}{N}(s - s_j), \tag{3.6}$$

and the derivative of C_j is

$$\frac{\mathrm{d}C_j}{\mathrm{d}s}(s_i) = \begin{cases} \dfrac{\pi}{N}(-1)^{i+j} \cot \dfrac{\pi}{N}(s_i - s_j) & \text{if } i \neq j \\ 0 & \text{if } i = j. \end{cases} \tag{3.7}$$

Then, equation (3.4) becomes

$$\sum_{j=1}^{N} \Gamma_{jk} w_j = 0 \qquad \text{for } k = 1, \ldots, N, \tag{3.8}$$

where the influence coefficients Γ_{jk} are now

$$\Gamma_{jk} = \begin{cases} \dfrac{1}{\xi_j - \xi_k} \left(\dfrac{\mathrm{d}z}{\mathrm{d}s} \right)_j + \dfrac{\mathrm{d}C_j}{\mathrm{d}s}(s_k) & \text{if } j \neq k \\ -\displaystyle\sum_{i=1, i \neq k}^{N} \dfrac{1}{\xi_i - \xi_k} \left(\dfrac{\mathrm{d}\xi}{\mathrm{d}s} \right)_i & \text{if } j = k. \end{cases} \tag{3.9}$$

The above algebraic system is solved iteratively using a generalized minimum residual method (GMRES). This variation of the conjugate gradient method for non-symmetric matrices works very well on the diagonally dominant matrices of (3.8) or the equivalent piecewise-linear implementation (Schultz *et al.* 1994) that we use for extreme waves. Fourth-order Runge–Kutta–Gill and Hamming predictor–corrector methods with an automatic step-size adjustment (controlled by a marching-error tolerance ϵ_t) were both used, with the predictor–corrector method showing the greater

https://doi.org/10.1017/S0022112098001773 Published online by Cambridge University Press

computational efficiency, especially for the higher-accuracy computations. Filtering as discussed in Schultz *et al.* (1994) may be necessary to calculate near-breaking travelling waves, although none was needed nor used here to obtain steep standing waves.

3.2. *Newton iteration method*

We start by considering static initial conditions with a deformed interface. Therefore, the standing wave solutions always have zero kinetic energy at its crest phase. In addition to the spatial and temporal periodicity, the inherent symmetries further simplify the solution procedure: the N unknowns of the initially stationary surface profile are reduced to $N/2+1$ due to spatial symmetry about the crest and trough. If a standing wave solution is initially stationary, the wave profile is again stationary at $t = T/2$ due to temporal symmetry. We thus require that each node returns to $\phi = 0$ at $t = T/2$. This ensures that the elevation profile repeats itself with a π-horizontal shift as we have verified for typical cases. Marching for one half-period also reduces the computational cost. An additional constraint on the initial conditions comes from any of the following: wave amplitude, amplitude of the first Fourier component, potential energy, or crest curvature. The resulting $N/2+2$ nonlinear algebraic equations are solved by the Newton–Raphson method (Schwartz & Vanden-Broeck 1979) for the $N/2+1$ unknown elevations and an unknown period T.

We restrict the number of nodes N to powers of two and use a FFT to spectrally estimate the spatial derivatives in the free surface conditions. The matrix problem is solved using a LINPACK conjugate gradient iterative technique. This technique solves the problem in $O(UVL)$ operations, where U is the number of unknowns, V is the number of equations, and L is the number of iterations. Both the influence matrix and the error vector are updated with each iteration. For most of the cases discussed herein, only three to five iterations are required. Even with a homogeneous initial guess, a typical solution for a non-singular matrix requires less than 10 iterations. The convergence of the spectral method is found (Schultz *et al.* 1994) to give essentially double precision (16 digit) machine accuracy with $N = 32$ and marching error 10^{-13} for moderate amplitude waves. Therefore, a marching-error tolerance $\epsilon_t = 10^{-10}$ and iteration-error tolerance $\epsilon_c = 10^{-8}$ are adopted. The error in the normalized energy is less than 3×10^{-10} in most calculations reported here.

As the initial iterate for the initial conditions, we use the second-order expansion for standing gravity waves:

$$\eta = a\cos x + \frac{a^2}{2}\cos 2x \quad \text{and} \quad \phi = 0. \tag{3.10}$$

The initial iterate for the period is

$$T = \frac{2\pi}{1 - a^2/8}. \tag{3.11}$$

The amplitude is *usually* fixed by the total energy density E (energy per wavelength), except in the neighbourhood of the highest waves. The total energy density E is of course conserved, and is given by the following integrals along one wavelength on the free surface:

$$E = E_p + E_k + E_s = \frac{1}{2}\int_0^{2\pi} \eta^2 \mathrm{d}x + \frac{1}{2}\int_0^{2\pi} \phi \frac{\partial \psi}{\partial s}\mathrm{d}s + \kappa\left[\int_0^{2\pi} \mathrm{d}s - 2\pi\right]. \tag{3.12}$$

These three terms – potential energy density (E_p), kinetic energy density (E_k), and surface-tension energy density (E_s) – are defined in such a way that all become zero at zero wave amplitude.

https://doi.org/10.1017/S0022112098001773 Published online by Cambridge University Press

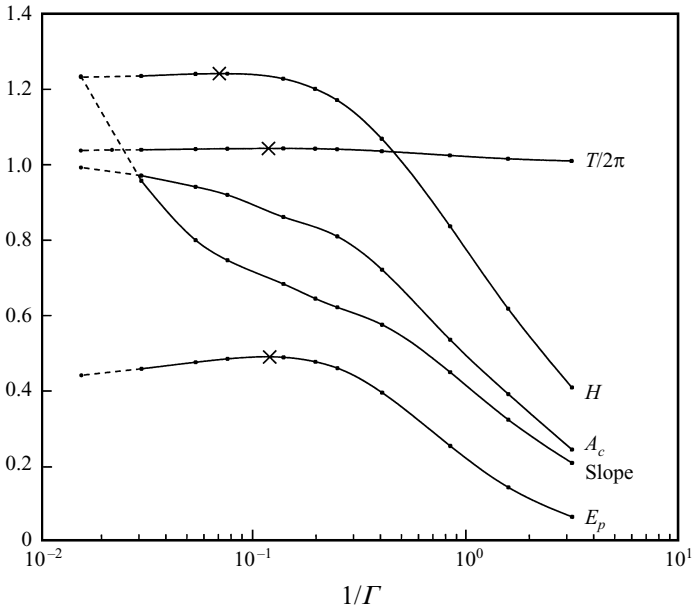


FIGURE 2. Gravity wave properties versus crest radius, $1/\Gamma$. T: wave period; A_c: crest acceleration; Slope: the maximum wave slope in the wave profile; $\times$ marks the maximum of the respective wave property. Dashed lines represent results from a finite-difference scheme rather than the spectral representation.

4. Steep gravity waves

4.1. *Wave properties*

We first discuss the non-monotonic behaviour of standing waves without surface tension. As demonstrated in both Schultz & Vanden-Broeck (1990) and Mercer & Roberts (1992), the dimensionless global wave properties, such as wave height $H = y_{max} - y_{min}$ at the moment the wave becomes stationary, wave energy E, and wave period T are not monotonic functions as the standing wave approaches its limiting form. A gravity standing wave is better characterized by a local property (in space and time) at the wave crest, such as crest acceleration A_c, crest curvature Γ, or the maximum wave slope near the crest. To study the limiting gravity waves, we choose crest curvature as the deciding parameter rather than the crest acceleration used by Mercer & Roberts (1992). As the crest radius decreases in figure 2, the maximum wave slope increases monotonically, and so does the crest acceleration. The total energy, wave period, and wave height all reach their maxima before the formation of the sharpest wave crest and then decrease.

At large crest curvature, the spectral method becomes less accurate because of the nearly singular behaviour at the crest. Therefore we use a finite-difference (piecewise-linear) estimate of (3.2) and obtain results valid to graphical accuracy for $1/\Gamma$ as small as that shown by the small-$1/\Gamma$ end of the dashed line in figure 2. Computational results with smaller crest radius have a normalized energy error larger than 10^{-6} with 64 nodes. The finite-difference prediction at $1/\Gamma = 1/30$ (where the solid and dashed lines meet in figure 2) is within graphic accuracy of the spectral method prediction. Table 1 shows that the maximum values of wave height, energy, and period obtained with a 64-node mesh agree with Mercer & Roberts (1992) to three significant digits. A convergence study shows that our values are accurate to at least the digits shown for

https://doi.org/10.1017/S0022112098001773 Published online by Cambridge University Press

	Global maxima			Limiting local properties		
	H_{max}	E_{max}	$T_{max}/2\pi$	A_c	θ(deg.)	Γ
Present study	1.2403	0.4882	1.0414	0.9923	78.0	64.6
Mercer & Roberts (1992)	1.2404	0.4885	1.0415	0.9800	89.4	—

TABLE 1. Comparison of limiting gravity-wave properties with Mercer & Roberts (1992). The limiting local properties represent the limit of accurate computations (in our case represented by the small-Γ end of the dashed line of figure 2. The maximum crest curvature is not available in Mercer & Roberts (1992). The limiting crest angle is represented by θ.

the maximum values. The maximum crest angle is the included angle obtained from the calculated maximum wave slope near the crest. Hence θ is twice the arctangent of the maximum slope.

In figure 3(a), the crest curvature continues to increase following the E_p, H curve beyond the maximum point ($E_p = 0.4882$). Adopting E_p as the determining parameter causes our calculation to jump from the branch with a more rounded crest to the branch with a sharper crest before reaching the maximum E_p. A superharmonic instability found by Mercer & Roberts (1992) occurs for solutions near the maximum E_p in figure 3(a), and therefore may correspond to the existence of two solutions at the same potential energy. The computations for sharper crests gradually become less reliable as the curve progresses past the maximum E_p. Figure 3(b) shows an essentially linear relationship between T and E_p for all wave steepnesses with zero surface tension. This strong correlation between E_p and the wave period T is also shown in figure 2 and both reach their maxima at the same crest curvature.

4.2. *Singularity formation at the crest*

The crest angle of a limiting form standing wave is often conjectured to be 90° as first suggested by Penney & Price (1952). They started their analysis by stating that the pressure must be a minimum at the surface as the fluid 'cannot withstand tension'. The limiting form would be such that the vertical pressure gradient at the crest is zero. The pressure gradient at the free surface was then expanded in a Taylor series about the crest to give

$$\mathrm{d}p = \frac{\partial p}{\partial x}\delta x + \frac{\partial p}{\partial y}\delta y + \frac{\partial^2 p}{\partial x^2}\frac{\delta x^2}{2} + \frac{\partial^2 p}{\partial y^2}\frac{\delta y^2}{2} + \frac{\partial^2 p}{\partial x \partial y}\delta x \delta y + \ldots = 0.$$

They then state that the first and fifth terms are zero because of symmetry and that the second term is zero for the 'tension' reason referred to above. Finally, they argue that at the moment of singularity formation, the fluid is temporarily stationary so the pressure satisfies the Laplace equation. This forces the remaining terms to satisfy

$$\delta x^2 = \delta y^2 \quad \text{or} \quad \delta x = \pm \delta y.$$

Hence, they expect a $\pm 45°$ slope on either side of the crest.

Taylor (1953) first questioned their analysis, in particular the lack of a temporal periodicity requirement, but his experiments were inconclusive. All analyses to date of the limiting crest form have neglected temporal periodicity and the unsteady nature of standing waves. In this respect, the analysis of Stokes (1880) for the limiting travelling waves is simpler because of the steady assumption. Schwartz & Whitney (1981)

https://doi.org/10.1017/S0022112098001773 Published online by Cambridge University Press

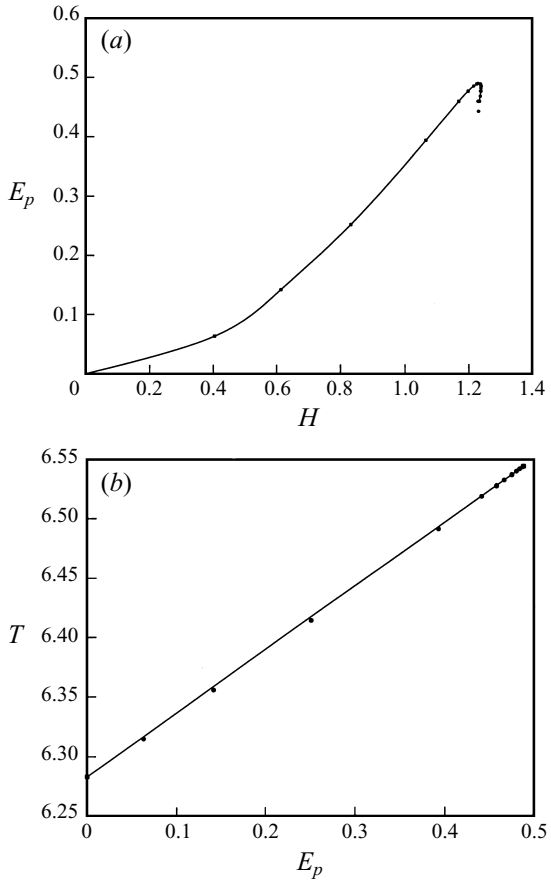


FIGURE 3. (*a*) E_p vs. wave height H, (*b*) wave period T vs. E_p for standing gravity waves. Dots in (*b*) correspond to the same data as those shown in (*a*). The line in (*b*) is a linear fit between the end points at zero E_p and at the maximum E_p.

pointed out that the regular expansion used by Penney & Price may be invalid if the crest is singular in the limiting form. However, extrapolation of Schwartz & Whitney's numerical results implies a square-root singularity, corresponding to the same 90° crest angle. These studies could not prove or disprove the 90° conjecture as their choice of expansion parameter ka reaches a maximum before the extremal values of the crest curvature and the crest angle are reached.

Using a denser node distribution at the crest ($0.5 < S < 0.8$) improves our calculation beyond the steepest wave calculated by Mercer & Roberts (1992) (table 1). In figure 2, the wave slope increases rapidly beyond one as the crest radius ($1/\Gamma$) approaches zero, while the crest acceleration A_c approaches one. Of the five quantities plotted in figure 2, the slope is the only one that appears singular as $\Gamma \to \infty$. This suggests the formation of a cusp.

The stationary profiles shown in figure 4(*a*) represent three different crest curvatures ($\Gamma = 10, 30, 64.6$). The profile changes only locally near the crest when the crest curvature approaches 64.6, the largest crest curvature we computed for zero surface tension. An enlarged view of the crest region (figure 4*b*) shows little change in crest elevation for $\Gamma > 30$, but the crest angle becomes smaller than 90°. This figure

https://doi.org/10.1017/S0022112098001773 Published online by Cambridge University Press

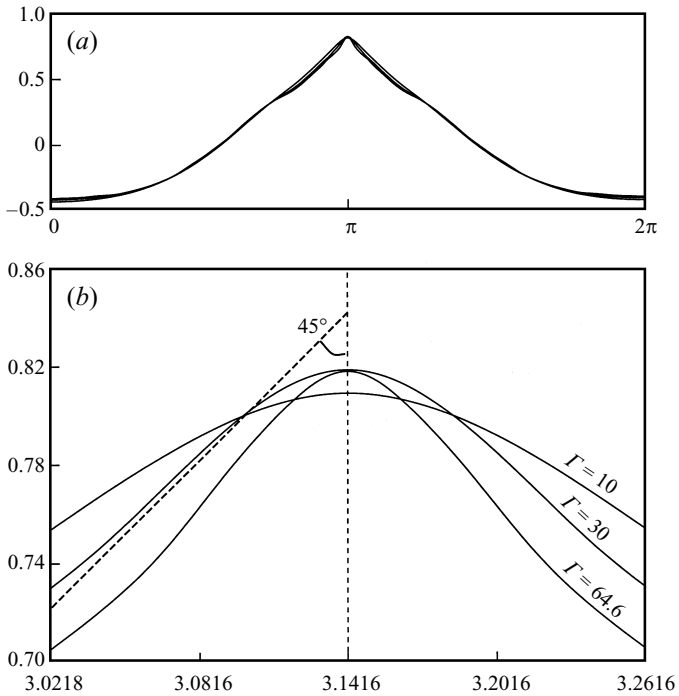


FIGURE 4. (*a*) Stationary profiles for different crest curvatures $\Gamma = 10, 30, 64.6$ with zero surface tension. (*b*) Magnified view of the crest. The 45° angle is included for comparison with the conjecture of Penney & Price.

also suggests a cusp singularity formation at the crest with further increase in crest curvature.

The min-max principle for harmonic functions shows that the pressure is smallest at the free surface (Schwartz & Whitney 1981). Then it is simple to conjecture that the pressure gradient goes to zero at the crest for the limiting case. This leads to a crest acceleration of $-g$ (free fall), as confirmed by extrapolations of the computations in figure 2. Neglecting gravity in the free surface conditions, Longuet-Higgins (1993) also shows possible cusp formation at finite time for certain initial conditions. To resolve the possible singularity in our calculation, we would need a singular mapping rather than just clustering nodes at the crest (Schultz, Lee & Boyd 1989).

Tsai & Jeng (1994) calculated standing waves in water of finite depth. Their computational approach is similar to Vanden-Broeck & Schwartz (1981) except that only the velocity potential was expanded in a double Fourier series while Vanden-Broeck & Schwartz expanded both the velocity potential and the surface elevation. A finite difference representation of the free surface elevation enabled Tsai & Jeng (1994) to calculate waves of higher amplitudes. The solution of the limiting wave was obtained assuming a crest acceleration of $-g$. Extending their numerical solution to infinite depth, they find a limiting crest with a 90° corner. Truncation errors contribute to the discrepancies with our results as well as those of Mercer & Roberts (1992) since Tsai & Jeng (1994) used only 24 nodes per wavelength and 24 time steps per wave period. They also provided a proof for the 90° limiting crest angle based upon the derivative of the Fourier solution as x approaches the wave crest. L'Hospital rule is used to estimate the wave slope in spite of the questionable convergence of the

https://doi.org/10.1017/S0022112098001773 Published online by Cambridge University Press

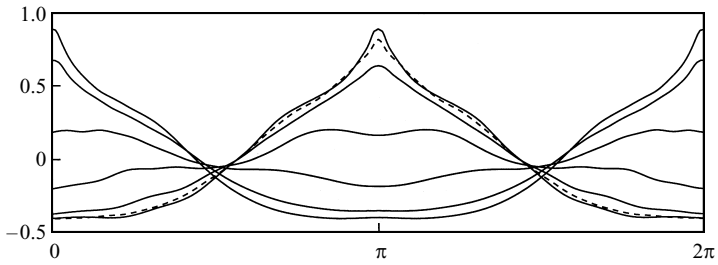


FIGURE 5. Surface profiles for a half wave cycle with a time interval of $0.1T$ for $\kappa = 0.0005$, $T = 3.268$, $E_p = 0.4748$, and $H = 1.29$. The wave profile with the sharpest crest ($\Gamma = 64.6$) in figure 4(*a*) for zero surface tension is shown as dashed line for comparison.

expansion near the singular crest. Therefore their argument suffers from the same difficulties encountered in the Taylor series expansion in Penney & Price's conjecture.

5. Weak capillary effect

The sharp crest of steep waves will not appear in experiments, even for large wavelengths, owing to surface tension effects. While the local effect at the crest is expected, we shall show that it has global implications. For instance, Taylor (1953) observed standing waves higher than predicted by Penney & Price (1952). We have already shown that Penney & Price (1952) overpredicted the limiting height that can be achieved without surface tension. In the following, we demonstrate that Taylor (1953) found $H_{max} > 1.24$ largely due to capillarity.

A typical half-cycle of surface profiles is shown in figure 5 for inverse Bond number $\kappa = 0.0005$. At the maximum wave elevation ($H = 1.29$ and $E_p = 0.4748$), the crest is more protuberant than the limiting gravity wave we calculated in § 4.2 (the dashed line in figure 5). A rounded crest and a large wave slope characterize most of the large-amplitude standing waves with large Bond number, demonstrating the importance of surface tension near the crest region.

Figure 6 shows the potential energy density versus wave height for $\kappa = 0.0001$ to 0.01 in addition to the $\kappa = 0$ curve reproduced from figure 3(*a*). These inverse Bond numbers correspond to wavelengths from 170 cm to 17 cm for pure water. The non-monotonic behaviour remains, but small surface tension extends both H_{max} and the maximum E_p. The difference between $\kappa = 0$ and $\kappa \neq 0$ only becomes significant close to the limiting height for a gravity wave. For all the results shown in figure 6, the surface-tension energy density E_s is small relative to the potential energy density E_p, i.e. $E_s/E_p = O(\kappa)$. However, small capillarity suppresses the crest singularity as shown in figure 5, and a gravity–capillary standing wave can be much higher than a gravity standing wave.

We obtain a maximum wave height of $H = 2.344$ at $\kappa = 0.002$ before our computation loses accuracy. This maximum height is almost twice the gravity-wave limit of $H = 1.240$. Therefore, it is not surprising that Taylor (1953) obtained steep standing waves at a similar inverse Bond number of $\kappa = 0.0027$. A calculated profile at $\kappa = 0.0027$ agrees well with the data from Taylor (1953) as shown in figure 7. Only 16 nodes are needed in the calculation and $y_{max} = 0.943$ is used to match Taylor's experiments. Unlike the prediction of Penney & Price, the highest gravity wave ($H_{max} = 1.2403$ from table 1) plotted in figure 7 is lower than the experimental results. Since this truncated expansion is applied to too high an amplitude, the agree-

https://doi.org/10.1017/S0022112098001773 Published online by Cambridge University Press

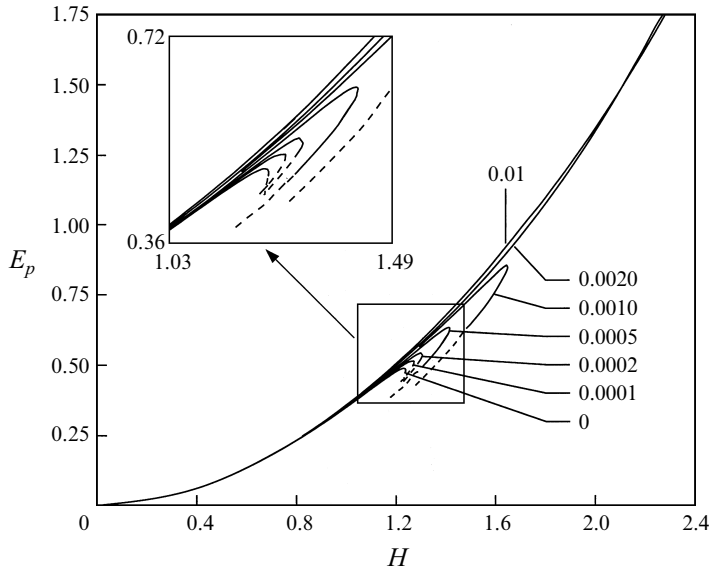


FIGURE 6. Potential energy versus wave height for different inverse Bond numbers κ; the number refers to the value of κ for each curve. Dashed lines represent results with increased error. An enlarged portion of the curves is shown in the insert.

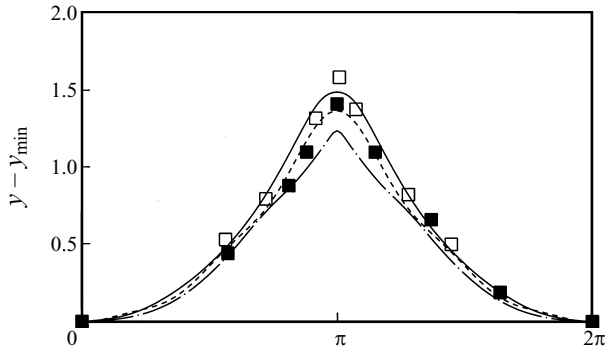


FIGURE 7. Comparison of wave profiles. The symbols are data taken from figures 11 and 12 of Taylor (1953). ——, A calculated gravity–capillary wave with $\kappa = 0.0027$, corresponding to a wavelength of 32.9 cm in Taylor's experiments; - - - - -, Penney & Price's (1952) gravity-wave solution at the overpredicted $H_{max} = 1.37$; — · —, the highest possible gravity wave ($H_{max} = 1.2403$, $\Gamma = 13$).

ment between Taylor's experiments and the expansion of Penney & Price (1952) is fortuitous. Schwartz & Whitney (1981) also pointed out fourth-order errors in Penney & Price's solution, although this error does not qualitatively change the comparison in figure 7.

The matching profile (solid line in figure 7) has a slightly different frequency than Taylor's experiments. Taylor (1953) stated that the maximum wave profile can be obtained only as a transitory phenomenon, and that periodic oscillation degenerates into three-dimensional motion after several periods. This is perhaps the result of his choice of tank aspect ratio. In § 6, we use Faraday-wave experiments to achieve both spatial and temporal periodicity to verify the predicted two-dimensional steep standing waves at small κ.

https://doi.org/10.1017/S0022112098001773 Published online by Cambridge University Press

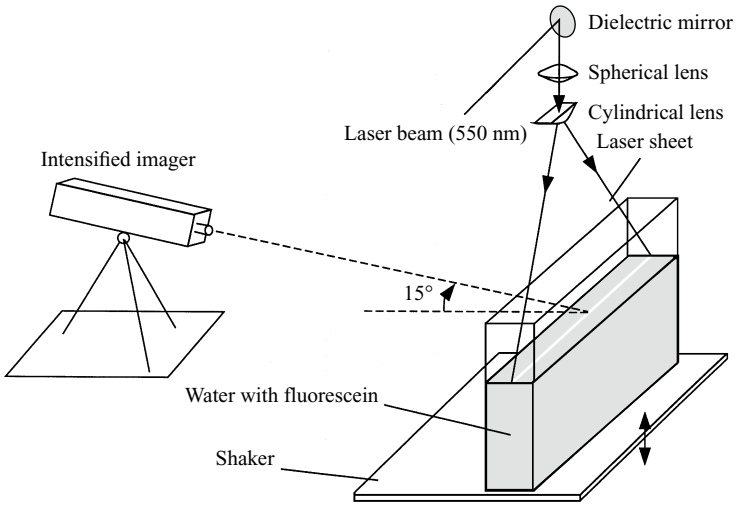


FIGURE 8. Experimental setup of the tank, illumination, and imaging system (not to scale). The spherical lens has a focal length of 1000 mm, the cylindrical lens has a focal length of 18 mm.

6. Experimental study

6.1. *Experimental setup and procedure*

Subharmonic standing waves (Faraday waves) can be generated on the water surface with forced vertical oscillation, i.e. the wave frequency is half the forcing frequency. The approach of Taylor (1953) uses horizontal (flap-type) wavemakers that change the wavelength periodically during a wave cycle. The extra superharmonics introduced by such wavemakers could cause instability in steep waves. Faraday-wave resonance is a 'cleaner' wave-generation mechanism as it better approximates spatial periodicity by fixed endwalls. This approach is adopted in Jiang *et al.* (1996) and Jiang, Perlin & Schultz (1998) and a similar setup used herein is shown in figure 8. The inner dimensions of the rectangular glass tank are 10.5 cm long, 1.7 cm wide and 30 cm deep. This 6.2 : 1 aspect ratio is chosen to eliminate transverse waves and maintain a two-dimensional wave field. The water depth is 15 cm, more than satisfying the deep-water condition.

A detailed description of the imaging system can be found in Jiang *et al.* (1996) and is only briefly described here. Using a 5 W Argon-Ion laser and attendant optics, a laser sheet is introduced from above the water and parallel to the longitudinal direction of the tank. With fluorescein dye present, the centreplane of the water body is illuminated by the laser sheet. We use a Kodak Ektapro CID intensified imager/recorder and a 100 mm camera lens to capture the wave profile. The optical axis is oriented perpendicular to the laser sheet and at about a 15° angle with respect to the mean water level to remove the meniscus effect. There is no significant image distortion in either direction. The imager is capable of recording full frames at a speed of up to 1000 Hz. Since the linear natural frequency for a 10.5 cm wavelength is $f_n = 3.91$ Hz, a 125 Hz recording speed is sufficient and provides 36 frames of surface profile per wave period. Each image is composed of 239 horizontal pixels by 192 vertical pixels with an average image resolution of 0.44 mm/pixel for this setup.

The tank is fixed to a programmable shaker, controlled by a Macintosh computer with National Instruments' LabVIEW software, data acquisition boards, and a feedback transducer for vertical displacements of the tank. This mechanically driven

https://doi.org/10.1017/S0022112098001773 Published online by Cambridge University Press

shaker is probably not the best choice for high-frequency oscillation, but has been found to produce satisfactory results for oscillations below 8 Hz, the upper frequency limit in the present experiments. Since deep water wave resonance curves are of the 'soft-spring' type (wave frequency decreases for increasing wave amplitude), only Faraday waves with subcritical frequency are reported here ($f < f_n$, f is the wave frequency and $2f$ is the forcing frequency). A Faraday wave at subcritical frequency can be excited either above or below the threshold forcing amplitude because of the hysteresis effect (Decent & Craik 1995). To reduce the forcing effect, most of the experimental data shown here are obtained below the threshold forcing amplitude (i.e. outside the neutral-stability curve). However, finite-amplitude disturbances are required to initiate Faraday waves below the threshold forcing. We achieve this initial condition by disturbing the surface with a Plexiglas plate before the forcing starts. This simple approach facilitates the generation of large-amplitude waves with the least forcing and therefore reduces the external forcing influence on steep waveforms. Once the wave is excited, we wait sufficiently long (typically more than 1000 wave cycles) to ensure temporal periodicity.

To avoid surface contamination, the tank is scrubbed before and after each use with ethyl alcohol. Our treated water is de-ionized, carbon-adsorbed, and filtered to maintain a surface tension of 72 dynes cm^{-1}, close to that for pure water at room temperature (23 °C). The surface tension decreases to about 71 dynes cm^{-1} after the addition of fluorescein. Contact-line constraints significantly influence the frequency of small-amplitude waves as shown by Jiang *et al.* (1996) and the references therein. Here, we study finite-amplitude waves where the contact line has much less influence. Because of the narrow tank geometry, the imaging plane must be accurately located at the centre of the tank to minimize the effect of menisci on the front and back glass walls. Although care is taken to maintain a clean tank, leaving the tank uncovered for several hours has little effect on the measured steep waves and hence the surface contamination effect is insignificant.

6.2. *Steep wave with weak capillary effect*

The forcing frequency $2f$ is varied between 6.8 Hz and 7.75 Hz (f/f_n from 0.870 to 0.992, $f_n = 3.91$ Hz) to obtain steep waves with a wavelength of 10.5 cm. Here, the frequency ratio f/f_n is equivalent to T_0/T in our calculation (§ 4) where $T_0 = 1.0$ is the dimensionless linear wave period. At each frequency ratio, as many as six different forcing amplitudes are applied (denoted by F hereafter). In figure 9, these experimental results agree qualitatively with the calculated resonance curve (§ 5). The prediction of Penney & Price (1952) for pure gravity wave is also included in figure 9 (dashed line). Even with an error at fourth order, their solution for nonlinear wave frequency is within graphical accuracy of the solution of Schwartz & Whitney (1981) and differs only slightly from our calculation with weak capillarity (solid curve) below its steepness limit. Their steepness limit (dashed line termination), however, is only half of the maximum steepness measured, $H/2\pi = 0.425$. Thus, the gravity-wave solution greatly underpredicts the maximum steepness at short wavelengths. This is consistent with our calculation in § 5. The predicted lowest frequency (solid line termination in figure 9) only represents the limit of accurate computation for the unforced waves. We expect to find standing waves closer to the limiting form with more refined grids and smaller time steps.

Figure 9 also demonstrate the effects of forcing amplitude on the wave steepness at certain frequencies. For example, the measured wave steepness at $f/f_n = 0.947$ (point A) is closest to the resonance curve of unforced waves with $F = 0.6$ mm,

https://doi.org/10.1017/S0022112098001773 Published online by Cambridge University Press

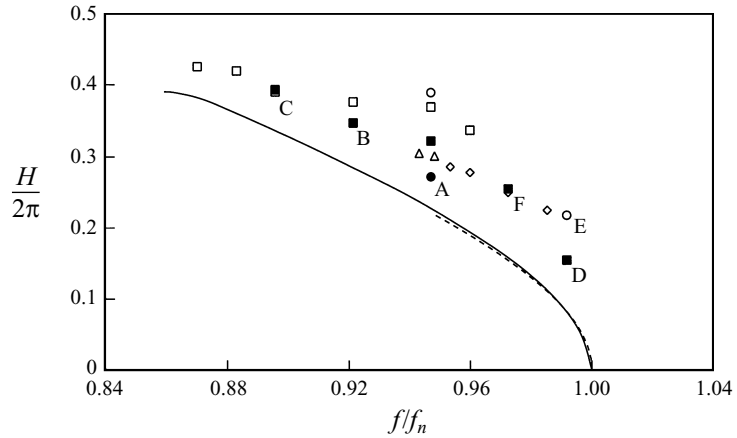


FIGURE 9. Resonance curve for κ=0.0265, corresponding to λ = 10.5 cm for water waves: ——, unforced computation from § 5; - - - - -, prediction of Penney & Price (1952) without surface tension effect. The symbols represent Faraday waves at different forcing amplitude F, ○, 1.3 mm; □, 1.1 mm; ■, 0.9 mm; △, 0.75 mm; ◇, 0.67 mm; ●, 0.6 mm. A–F denote data points corresponding to images in figures 10 to 12.

i.e. the smallest forcing amplitude of those applied. It becomes difficult to further reduce F at these frequencies and still excite the subharmonic wave since more time is required to reach a steady limit cycle. Also, a minimum forcing amplitude is required to overcome the viscous threshold. Forced standing waves of wavelength λ, either by direct excitation or by subharmonic resonance, can be described by two independent parameters: forcing amplitude and forcing frequency. Once a wavelength λ is chosen, free standing waves have only one parameter: wave amplitude or wave frequency. This difference between forced and free waves is responsible for the data scatter in figure 9 at different forcing amplitudes. Furthermore, the forced wave profiles are closer to the natural (free) waves when the forcing amplitude is small.

A set of stationary profiles for different forcing frequencies is shown in figure 10. The three experimental profiles in figures 10(*a*) to (*c*) correspond to the data points A to C in figure 9. Each profile corresponds to the smallest forcing amplitude at that forcing frequency. In all three experiments, the wave reaches the displayed profile with almost-zero kinetic energy (the profile changes little in a short time interval) and the maximum wave elevation at the tank centre. From figure 10(*a–c*), the wave height increases and the crest becomes flatter with a steep slope to each side. The surface slope near the crest is so steep in figure 10(*c*) that the re-emitted laser light is significantly reduced and the surface profile appears discontinuous in the laser-sheet image. The calculated waves at the same frequency are shown in the second column of figure 10 with the same scale as the experimental results. The calculated wave heights are less than those obtained in the experiments as already shown in figure 9. With the present nodal displacement and Jacobian procedure, we cannot calculate solutions where $\partial\eta/\partial x$ is locally as large as in the laser-sheet image of figure 10(*c*). In addition, only 16 nodes or 32 nodes are used in our calculation to avoid resonance with small ripples ($1/\kappa \approx 38$) as discussed in § 6.3. However, the calculated profile with large wave slope and flat wave crest agrees qualitatively with the measured wave profile.

https://doi.org/10.1017/S0022112098001773 Published online by Cambridge University Press

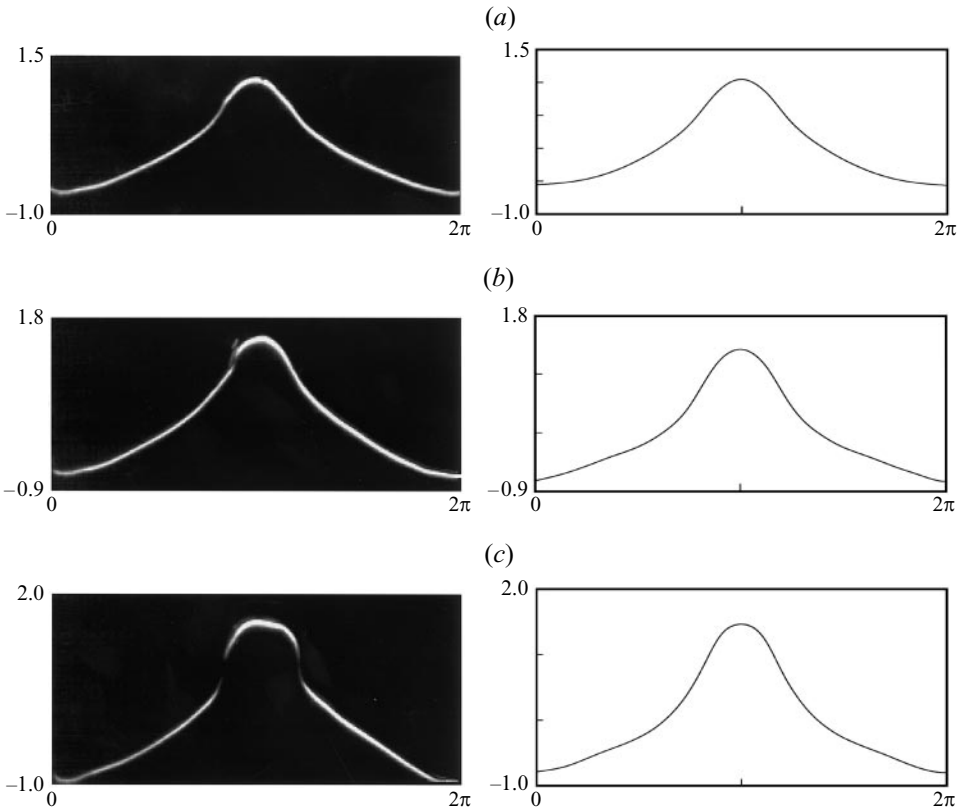


FIGURE 10. Comparison of wave profiles with $E_k = 0$ ($\kappa = 0.0265$). The left-hand column profiles are laser-sheet images of Faraday waves with (*a*) $f = 3.70$ Hz ($f/f_n = 0.947$), $F = 0.6$ mm; (*b*) $f = 3.60$ Hz ($f/f_n = 0.922$), $F = 0.9$ mm; (*c*) $f = 3.50$ Hz ($f/f_n = 0.896$), $F = 0.9$ mm. The laser-sheet images of (*a*) to (*c*) correspond to data point A to C in figure 9. The right-hand column presents the calculated profiles at the same frequency ratios.

6.3. *Temporal asymmetry and ripple generation in steep Faraday waves*

As shown in the previous section, qualitative agreement between free standing waves and Faraday waves is achieved when the excitation amplitude is small. A large wave steepness can be obtained by simply increasing forcing amplitude, although it no longer follows the theoretically predicted resonance curve (figure 9). A large forcing amplitude generates different wave forms as the external forcing alters the mode interaction in a standing-wave system. Overdriven Faraday waves in our experiment exhibit two major differences with the calculation of free, inviscid standing waves: temporal-symmetry breaking and ripple formation.

Figure 11 shows two sets of images for the same wave frequency, $f = 3.875$ Hz, but with two different forcing amplitudes (data points D and E in figure 9). Three different phases in a wave cycle are displayed with the phase of maximum crest elevation designated by $t = 0$. At a small forcing amplitude $F = 0.9$ mm (figure 11*a*), the time-reversal symmetry is approximately conserved – the wave assumes the same profile during the ascending ($t = -28$ ms) and the descending phases ($t = 28$ ms). This temporal symmetry, however, is broken at a larger forcing amplitude $F = 1.3$ mm (figure 11*b*). The sharper crest at $t = -28$ ms is contrasted with a much flatter crest at $t = 28$ ms. A similar observation in Jiang *et al.* (1996) has been attributed to

https://doi.org/10.1017/S0022112098001773 Published online by Cambridge University Press

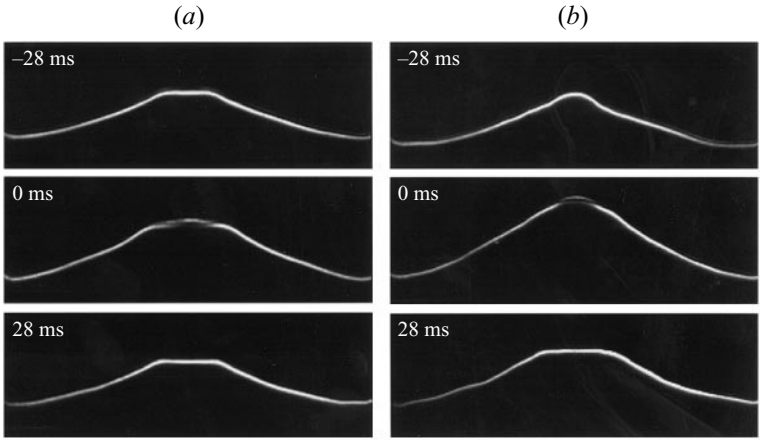


FIGURE 11. Temporal symmetry breaking at $f = 3.875$ Hz ($f/f_n = 0.992$). (*a*) $F = 0.9$ mm, (*b*) $F = 1.3$ mm. The maximum steepness obtained at 0 ms for (*a*) and (*b*) corresponds to data points D and E in figure 9, respectively.

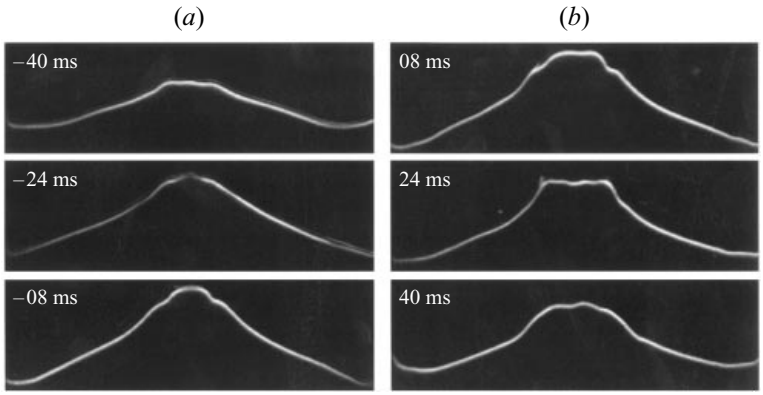


FIGURE 12. Ripple formation on a standing wave during a quarter wave period. The maximum elevation ($t = 0$) is not shown. $F = 0.9$ mm, $f = 3.8$ Hz ($f/f_n = 0.973$). This wave corresponds to data point F in figure 9.

resonance between the first two temporal harmonics when the forcing parameters are well within the neutral-stability curve. Both phenomena are related to the mode interactions of standing waves introduced by large external forcing.

At $f = 3.8$ Hz and $F = 0.9$ mm, the forced wave height is 60% higher than predicted for the free standing wave (see data point F in figure 9). Consecutive wave profiles during a quarter wave period (figure 12) exhibit a crest instability. The profile is relatively smooth before the central elevation reaches its maximum value (again corresponding to $t = 0$). The crest rapidly becomes flat during the decreasing elevation phase ($t = 24$ ms) and small ripples develop with wavelengths about 3 mm to 6 mm. They disappear when the wave elevation decreases further (not shown) but reappear in the next cycle. At $f = 3.7$ Hz ($f/f_n = 0.947$) and a larger forcing amplitude $F = 1.3$ mm, we also observe protuberance at the crest similar to some profiles seen by Taylor (1953).

The cyclic appearance of ripples in figure 12 is unlikely to be a result of a Rayleigh–Taylor instability even though the crest acceleration is higher than the gravitational

https://doi.org/10.1017/S0022112098001773 Published online by Cambridge University Press

acceleration based on our calculation.† Based on capillary–gravity wave theory, Wilton ripples occur for inverse Bond number $\kappa = 1/N$ where the fundamental harmonic has resonant interaction with its Nth spatial harmonic. Therefore the solutions at these critical values are not unique. This type of resonance is more likely to occur here as $\kappa = 0.0265 \approx 1/38$ is consistent with the observed 3 mm ripple wavelength. The present calculation does not attempt to capture the solutions with these ripples. Instead, this non-uniqueness problem is avoided by using a small number of nodes to exclude the resonant superharmonics. A more sophisticated Jacobian procedure is required to resolve all the solution branches when higher-order harmonic resonances occur.

However, the agreement in figure 10 between numerics and experiments is not coincidental. For those solutions with strong resonant ripples, the resonance curves should be different from that for the solution without ripples. As our experiments approximately follow the calculated resonance curve in figure 9, Faraday waves should resemble the predicted free standing waves that neglect the small resonant ripples. Furthermore, the free-surface boundary layer causes a viscous damping proportional to k^2 in the experiments, where k is the wavenumber. This viscous damping helps to stabilize the standing wave with respect to superharmonic disturbances.

7. Concluding remarks

A spectral boundary-integral method has been used to study standing waves with and without surface tension. Numerical experiments have found standing waves that maintain both spatial and temporal periodicity. We show that the global wave properties, including wave period, height, and total energy, become non-monotonic as the standing gravity wave approaches its limiting form, therefore providing a complementary analysis to Mercer & Roberts (1992). As the crest radius goes to zero, the crest acceleration goes to the gravitational limit. In the process, the maximum wave slope grows rapidly beyond one. Using denser nodes around the crest, we have found crest angles smaller than 90°, contrary to the conjecture of Penney & Price (1952) and Schwartz & Whitney (1981). This suggests eventual singularity at the crest, possibly a cusp.

We have demonstrated that the surface tension effect can extend the limiting wave height for standing waves. However, the non-monotonic behaviour persists for weak surface tension ($\kappa < 0.001$). Standing water waves with small surface tension can be extremely high and a wave steepness of $H/2\pi = 0.38$ is easily achieved for $\kappa = 0.0027$, the inverse Bond number for the experiments of Taylor (1953). The findings of Taylor (1953) can only be explained by the effect of surface tension. Capillarity becomes important when the wave height approaches and then exceeds the gravity-wave limit, and inhibits a possible singularity at the crest. Most of the steep gravity–capillary standing waves feature a flat or protuberant crest.

Using Faraday-wave resonance and a tank of 6.2 : 1 aspect ratio, we found similar two-dimensional standing waves in laboratory experiments. For a wavelength of 10.5 cm ($\kappa = 0.0265$), we find a maximum steepness of $H/2\pi = 0.425$, corresponding to a nonlinear wave frequency of 3.4 Hz (the linear wave frequency is 3.91 Hz). Wave profiles measured using a laser-sheet technique show rounded crests and large slopes close to the crest. Both the resonance curve and the wave profiles qualitatively agree

† For a clean water surface under free fall, surface tension stabilizes disturbances below a cut-off wavelength of 1.7 cm (Chandrasekhar 1961). The observed ripples have much shorter wavelengths.

https://doi.org/10.1017/S0022112098001773 Published online by Cambridge University Press

with our calculations when the effect of forcing amplitude is minimal. We appear to be the first to observe such steep standing waves in the laboratory.

For overdriven Faraday waves (large external forcing), time-reversal symmetry is broken and ripples form at certain phases of the oscillation. The temporal asymmetry reflects the strong forcing that alters the mode interaction as shown in Jiang *et al.* (1996). The ripple generation is related to the existence of multiple solutions of gravity–capillary waves at certain critical inverse Bond numbers, and is neglected in the present calculation for weak capillarity. These highly nonlinear Faraday waves require more elaborate analysis that considers both the nonlinearity and the force-dissipation balance.

The work at the University of Michigan was supported by Naval Research Laboratory Contract No. N00014-85-K-Z019, ONR Ocean Engineering Division Contract N00014-87-0509, N00014-93-1-0867, ONR URI – Program in Ship Hydrodynamics at the University of Michigan contracts No. N000184-86-K-0684 and N00014-87-K-2021, and partially under the ONR URI – Ocean Surface Processes and Remote Sensing at the University of Michigan, contract number N00014-92-J-1650. The work at the University of Wisconsin was supported in part by the National Science Foundation.

REFERENCES

Amick, C. J. & Toland, J. F. 1987 The semi-analytic theory of standing waves. *Proc. R. Soc. Lond.* A **411**, 123–137.

Baker, G. R., Meiron, D. I. & Orszag, S. A. 1982 Generalized vortex methods for free-surface flow problems. *J. Fluid Mech.* **123**, 477–501.

Boyd, J. 1989 *Fourier and Chebyshev Spectral Methods.* Springer.

Bridges, T. J. & Dias, F. 1990 An analysis of two-dimensional water waves based on O(2) symmetry. *Nonlinear Analysis* **14**, 733–764.

Chandrasekhar, S. 1961 *Hydrodynamic and Hydromagnetic Instability*. Clarendon.

Concus, P. 1962 Standing capillary-gravity waves of finite amplitudes. *J. Fluid Mech.* **14**, 568–576.

Debiane, M. & Kharif, C. 1996 A new limiting form for steady periodic gravity waves with surface tension on deep water. *Phys. Fluids* **8**, 2780–2782.

Decent, S. P. & Craig, A. D. D. 1995 Hysteresis in Faraday resonance *J. Fluid Mech.* **293**, 237–268.

Hogan, S. J. 1980 Some effects of surface tension on steep water waves. Part 2. *J. Fluid Mech.* **96**, 417–445.

Jiang, L., Perlin, M. & Schultz, W. W. 1998 Period tripling and energy dissipation of breaking standing waves. *J. Fluid Mech.* **369**, 273–299.

Jiang, L., Ting, C.-L., Perlin, M. & Schultz, W. W. 1996 Moderate and steep Faraday waves: instabilities, modulation and temporal asymmetries. *J. Fluid Mech.* **329**, 275–307.

Longuet-Higgins, M. S. 1975 Integral properties of periodic gravity waves of finite amplitude. *Proc. R. Soc. Lond.* A **342**, 157–174.

Longuet-Higgins, M. S. 1993 Highly accelerated, free-surface flows. *J. Fluid Mech.* **248**, 449–475.

Mercer, G. N. & Roberts, A. J. 1992 Standing waves in deep water: their stability and extreme form. *Phys. Fluids* A **4**, 259–269.

Mercer, G. N. & Roberts, A. J. 1994 The form of standing waves on finite depth water. *Wave Motion* **19**, 233–244.

Penney, W. G. & Price, A. T. 1952 Finite periodic stationary gravity waves in a perfect fluid. *Proc. R. Soc. Lond.* A **244**, 254–284.

Rayleigh, Lord 1915 Deep water waves, progressive or stationary, to the third order of approximation *Proc. R. Soc. Lond.* A **91**, 345–353.

Roberts, A. J. 1983 A stable and accurate numerical method to calculate the motion of a sharp interface between fluids *IMA J. Appl. Maths* **31**, 13–35.

Schultz, W. W., Huh, J. & Griffin, O. M. 1994 Potential energy in steep and breaking waves. *J. Fluid Mech.* **278**, 201–228.

https://doi.org/10.1017/S0022112098001773 Published online by Cambridge University Press

Schultz, W. W., Lee, N.-Y. & Boyd, J. P. Chebyshev pseudospectral method of viscous flows with corner singularities. *J. Comput. Phys.* **94**, 30–58.

Schultz, W. W. & Vanden-Broeck J. M. 1990 Computations of nonlinear standing waves. *Bull. Am. Phys. Soc.* **35**, 2290.

Schwartz, L. W. & Fenton, J. D. 1982 Strongly nonlinear waves *Ann. Rev. Fluid Mech.* **14**, 39–60.

Schwartz, L. W. & Vanden-Broeck, J.-M. 1979 Numerical solution of the exact equations for capillary-gravity waves *J. Fluid Mech.* **95**, 119–139.

Schwartz, L. W. & Whitney, A. K. 1981 A semi-analytical solution for nonlinear standing waves in deep water *J. Fluid Mech.* **107**, 147–171.

Stokes, G. G. 1880 Supplement to a paper on the theory of oscillatory waves. In *Mathematical and Physical Papers*, vol. 1, pp. 314–326.

Tadjbakhsh, I. & Keller, J. B. 1960 Standing surface waves of finite amplitude. *J. Fluid Mech.* **8**, 442–451.

Taylor, G. I. 1953 An experimental study of standing waves. *Proc. R. Soc. Lond.* A **218**, 44–59.

Tsai, C.-P. & Jeng, D.-S. 1994 Numerical Fourier solutions of standing waves in finite water depth. *Appl. Ocean Res.* **16**, 185–193.

Vanden-Broeck, J.-M. 1984 Nonlinear gravity-capillary standing waves in water of arbitrary uniform depth. *J. Fluid Mech.* **139**, 97–104.

Vanden-Broeck, J.-M. & Schwartz, L. W. 1981 Numerical calculation of standing waves in water of arbitrary uniform depth. *Phys. Fluids* **24**, 812–815.

Vinje, T. & Brevig, P. 1981 Numerical simulation of breaking waves. *Adv. Water Resources* **4**, 77–82.

https://doi.org/10.1017/S0022112098001773 Published online by Cambridge University Press